ADVANCED FUNCTIONAL MATERIALS
www.afm-journal.de

Quantum-Defect-Minimized, Three-Photon-Pumped Ultralow-Threshold Perovskite Excitonic Lasing

*Jianhui Sun, Zhedong Zhang, Yongyi Chen, Meng Qiu, Wei Jin, Cun-Zheng Ning, Henry J. Snaith, Alex K.-Y. Jen, and Dangyuan Lei**

Three-photon-pumped (3PP) excitonic lasing in inorganic semiconductor quantum dots (QDs) is of particular importance for near-infrared biophotonics and optical communications. However, the implementation of such lasers has been hindered severely by the required high pump thresholds. Here, 3PP excitonic lasing of all-inorganic cesium lead bromide perovskite QDs ($CsPbBr_3$ PQDs) embedded in a whispering-gallery microcavity is demonstrated, and achieving a record low threshold of 3 mJ cm^{-2} by tuning the 3P pump energy in resonance with the *S* exciton state. Wavelength-dispersive Z-scan spectroscopy reveals that such reduced lasing threshold is attributed to the exciton resonance enhanced multiphoton absorption, which, as disclosed by the kinetics analysis of transient absorption spectroscopy (TAS), leads to the appearance of net gain at a pump fluence as low as 2.2 mJ cm^{-2}, corresponding to an average *S* exciton population of 1.5. A microscopic model incorporating the quantum master equation reproduces the TAS results and provides the intrinsic parameters of biexciton relaxation for lasing. The 3PP resonant excitonic transition is the most favored multiphoton pumping process that minimizes quantum defect (6.8% of the pump photon energy) to realize optical gain at low threshold, marking a major step toward using all-inorganic perovskite QDs for on-chip integrated microlasers and multiphoton bioimaging.

1. Introduction

Three-photon-pumped (3PP) stimulated emission from inorganic semiconductor QDs enables coherent frequency up-conversion with merits such as ultrahigh photostability and large multiphoton absorption cross-sections in comparison to organic counterparts.[1–6] It is particularly important for near-infrared-pumped bioimaging and optical communication since the excitation wavelengths lie in the near-infrared biological transparency window[4,7] and also in the low-loss transmission region of optical fibers.[8,9] In principle, 3PP lasing requires the optical gain media with extraordinarily large 3P absorption cross-sections and ultrahigh photoluminescence (PL) quantum yields. Recently, all-inorganic colloidal perovskite quantum dots (PQDs) like $CsPbBr_3$ have been found to show infrared two-photon (2P) absorption cross-sections[10–12] about two orders of magnitude larger than that

J. Sun
College of Physical Science and Technology
Heilongjiang University
Harbin 150080, China

J. Sun, D. Lei
Department of Applied Physics
Hong Kong Polytechnic University
Hong Kong SAR China
E-mail: dangylei@cityu.edu.hk

Z. Zhang
Department of Physics
City University of Hong Kong
83 Tat Chee Avenue, Kowloon, Hong Kong SAR China

Y. Chen
State Key Laboratory of Luminescence and Applications, Changchun Institute of Optics, Fine Mechanics and Physics
Chinese Academy of Sciences
Changchun 130033, China

The ORCID identification number(s) for the author(s) of this article can be found under https://doi.org/10.1002/adfm.202401247

DOI: 10.1002/adfm.202401247

M. Qiu, W. Jin
Department of Electrical Engineering
Hong Kong Polytechnic University
Hung Hom, Kowloon, Hong Kong SAR China

C.-Z. Ning
School of Integrated Circuits and Optoelectronic Chips
Shenzhen Technology University
Shenzhen 518118, China

H. J. Snaith
Department of Physics
Clarendon Laboratory
University of Oxford
Oxford OX1 3PU, UK

A. K.-Y. Jen
Department of Materials Science and Engineering
Department of Chemistry
and Hong Kong Institute of Clean Energy
City University of Hong Kong
83 Tat Chee Avenue, Kowloon, Hong Kong SAR China

D. Lei
Department of Materials Science and Engineering
Center for Functional Photonics and Hong Kong Branch of National Precious Metal Material Engineering Research Center
City University of Hong Kong
83 Tat Chee Avenue, Kowloon, Hong Kong SAR China

of conventional II-VI group semiconductor QDs.[13,14] Despite this exotic property, it has remained a great challenge to reach near-infrared 3PP population inversion in these materials because their 3P absorption cross-sections are substantially smaller than the one-photon (1P) and 2P processes. For this reason, earlier investigations of all-inorganic PQDs mainly focused on the 1PP and 2PP amplified spontaneous emission (ASE) and lasing,[15–18] and the 3PP lasing still remains elusive.

It is well known that optical absorption in semiconductor QDs can be enhanced through excitonic excitations, particularly for excitons with stronger oscillator strengths.[19] Therefore, it is prospected that the 3P absorption of $CsPbBr_3$ PQDs can be significantly leveraged through a single exciton resonance matching three times the pump photon energy. In addition, resonant optical pumping of the gain medium is an attractive path for quantum-defect-free lasing.[20–22] Since the infrared pumping energy is triplicated exactly towards the PQD exciton radiation energy under the quantum-defect-free pumping, it therefore minimizes the amount of energy dissipation through phonons. This can inhibit the lattice temperature rising of the PQDs and thus prevent potential photothermal damage as well as radiance efficiency losses, thereby improving the stability of laser devices. Despite such unparalleled merits, the development of PQDs-based 3PP laser devices has been substantially hindered by their poor stability: Most polar solvents deleteriously quench the PL signals of halide PQDs because their ionic crystal structures can be easily etched in humid environment,[17,23] which becomes even worse under intense pumping. Therefore, high quality factor (high-Q) optical cavities are necessary to make compatible incorporation of PQDs in a protective environment.

Here, we demonstrate 3PP excitonic lasing from $CsPbBr_3$ PQDs, which exhibits a record low pump threshold in comparison with other all-inorganic semiconductor QDs (see Table S2, Supporting Information). First, we combine 1P, 2P and 3P absorption spectroscopies to determine the parity-allowed excitonic transitions of the PQDs, which fulfill respective optical selection rules and agree with our quantum mechanical calculations. Second, we show the 2PP and 3PP excitonic lasing thresholds of the PQDs incorporated in bottle-like optical microcavities supporting whispering-gallery modes reach minima when the 2P and 3P pump energies approach the *P* and *S* excitonic states of the PQDs at which the nonlinear absorption cross-sections exhibit maxima. Third, an ultrafast pump-probe spectroscopic signal reveals that the excitonic radiation reaches an optical net gain at a 3P pump fluence of 2.2 mJ cm^{-2} with the population inversion lasting for 18 ps, whilst further increasing pump fluence leads to whispering-gallery-mode-supported excitonic lasing with a threshold ≈3 mJ cm^{-2}. A quantum mechanical model incorporating master equation can produce the results in perfect agreement with the ultrafast pump-probe measurement. The intrinsic parameters of excitons in PQDs such as biexciton damping and non-radiative decay rates are found, manifesting the universality for all the pump fluences in the experiments. Finally, we demonstrate that the 3PP exciton laser can be switched between multiple and single modes, both exhibiting long-lived output stability, by simply adjusting the cavity diameter with an easy-to-implement all-solution-processed method. Briefly, our enhanced fundamental understanding of the rich excitonic transitions in the PQDs, the methodology developed for controlling lasing characteristics, and the ultralow-threshold 3PP excitonic lasing and exceptional output stability we have observed, achieve a great step toward practical use of all-inorganic PQDs for near-infrared-pumped bioimaging and optical communication.

2. Results and Discussion

2.1. Morphological Characterization and Optical Spectroscopies of $CsPbBr_3$ PQDs

The transmission electron microscopy (TEM) micrograph in **Figure 1a** shows that the $CsPbBr_3$ PQDs synthesized in the study exhibit an orthorhombic shape inherited from their crystallization in the cubic perovskite phase. The lattice fringe pattern of a single $CsPbBr_3$ PQD shows a lattice spacing of 0.58 nm, corresponding to the (100) plane of the perovskite phase and demonstrating good crystallinity. The average size of the PQDs was measured to be 9.2±1.2 nm along their edges (see the size distribution analysis in Figure 1b and the TEM image in Figure S1, Supporting Information), close to the bulk Bohr exciton diameter (7 nm) for the $CsPbBr_3$ PQDs,[24] at which the quantum confinement effect discretizes the electron and hole energy levels. As a result, the two lowest levels in conduction band, S_e and P_e, and the two highest levels in valence band, S_h and P_h, are resolved, responsible for rich excitonic transitions in the PQDs.[25]

Since the rich electronic transitions between discrete energy levels of low-dimensional semiconductors obey different optical selection rules,[26] we essentially combine 1P, 2P, and 3P absorption spectroscopies to obtain a complete scenario of allowed excitonic transitions in the $CsPbBr_3$ PQDs. In Figure 1c, the 1P absorption spectrum of the PQDs shows, right above the band edge, two shallow peaks ≈507 nm and 470 nm, corresponding to the transitions $S_h \rightarrow S_e$ and $P_h \rightarrow P_e$, respectively, in consistence with the results obtained by transient absorption spectroscopy in Figure S2 (Supporting Information). However, the 1P absorption spectrum cannot resolve the energy splitting between S_e and P_e (and between S_h and P_h). This requires the use of 2P absorption spectroscopy to access a completely different manifold of excitonic transitions, i.e., $S_h \rightarrow P_e$ and $P_h \rightarrow S_e$. To this end, we carried out wavelength-dispersive open-aperture *Z*-scan nonlinear spectroscopies on the PQDs in toluene over the pump wavelength ranging from 750 to 1650 nm, enabling to probe the excitonic dark states absent in the 1P absorption. In order to measure the 2P and 3P absorptions, we make use of the property that the absorption cross-section increases as a higher-order power law of the photon intensity. With an excitation beam focusing on a position of fixed size, we scan the sample through this focal point to record the change in the transmission of the probe beam of the same wavelength. As dictated by the angular momentum associated with the exciton wavefunction, the excitonic 2P absorption obeys different selection rules, which normally allow hot excitons to reach higher-lying states that are parity-forbidden in 1P and 3P absorption processes.[4,27] These selection rules have been corroborated in near-spherical semiconductor QDs and anisotropic nanorods.[28,29] Indeed, the wavelength-dependent 2P absorption cross-section spectrum shown in Figure 1d exhibits a resonant peak at ≈970 nm, corresponding to a 2P energy of 2.557 eV, which lies at a higher energy than the lowest-energy 1P absorption peak at 2.446 eV (507 nm), indicating an energy splitting of 111 meV

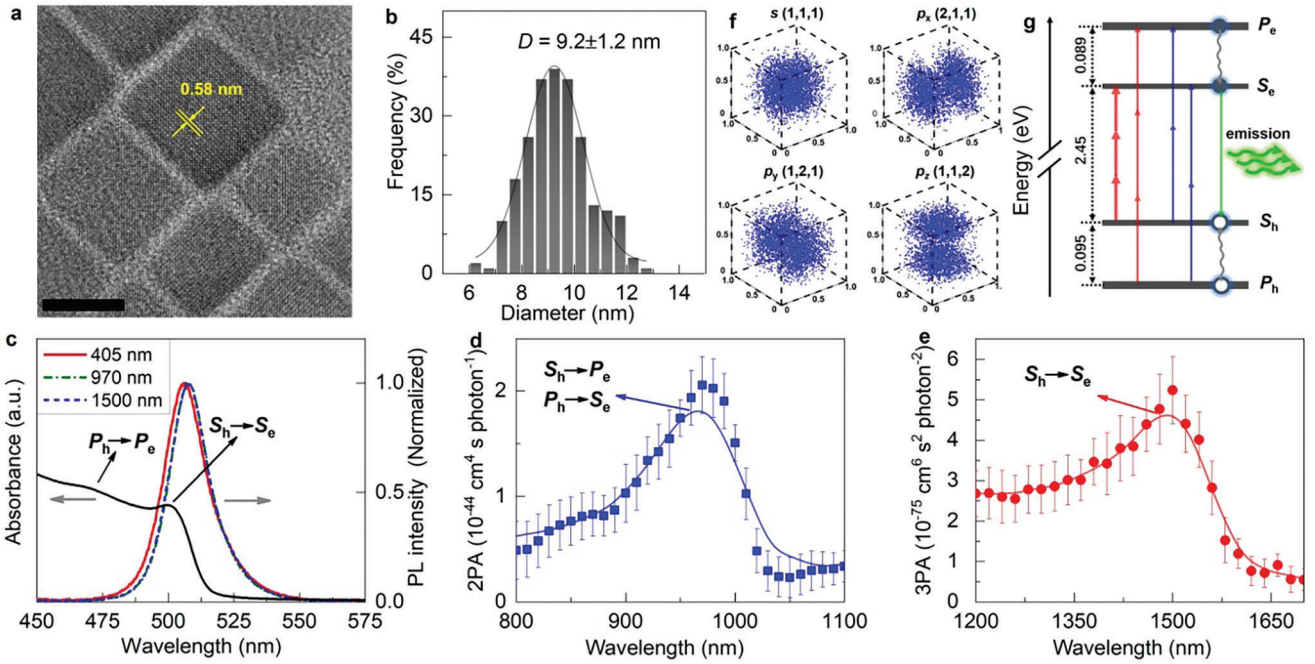

Figure 1. a) Transmission electron microscopy (TEM) micrograph of the PQDs with a PQD showing the (100) lattice plane with lattice spacing of 0.58 nm. The black scale bar is 10 nm. b) Histogram statistics of the PQD size distribution. c) 1P absorption spectrum (black) and PL spectra of the PQDs in toluene under 1P (CW 405 nm, cyan), 2P (fs 970 nm, red) and 3P (fs 1500 nm, orange) excitations. d,e) Wavelength-dependent 2P (d) and 3P (e) absorption cross-sections derived from *Z*-scan measurements. Error bars represent standard deviation of the fitting results. f) Calculated real-space distribution of the *S* and *P* exciton wave functions in a $CsPbBr_3$ PQD using a cubic box model with an infinite potential barrier. g) Jablonski diagram of allowed 2P (blue lines) and 3P (red lines) excitonic transitions in the PQD. Upon excitation to the P_e state through either process, the PQD undergoes fast relaxation to the S_e state through vibrational damping and gives rise to 2P or 3P PL.

between the S_e and P_e states. In contrast, the selection rules for 3P absorption are the same as that for 1P absorption because they both correspond to the transitions between parity-opposite states. Consequently, the 3P absorption cross-section spectrum in Figure 1e exhibits a resonant peak at 1500 nm, equivalent to a 3P energy of 2.480 eV, almost the same as the 1P absorption peak (2.446 eV). The 2P and 3P absorption cross-sections of the $CsPbBr_3$ QDs are 1.88×10^{-44} cm^4 s photon^{-1} at 970 nm and 5.10×10^{-75} cm^6 s^2 photon^{-2} at 1500 nm (extracted from the Z-scan responses in Figure S3, Supporting Information). The 2P absorption cross-sections quantify the probability of this process occurring in a QD, while 3P absorption is a similar nonlinear optical process, but it involves the simultaneous absorption of three photons. The 3P absorption cross-section of $CsPbBr_3$ QDs is smaller than that of the 2P absorption cross-section. This is because the 3P absorption requires the simultaneous fulfillment of energy and momentum conservation conditions for three photons, whereas the 2P absorption requires for two photons only. Due to the more stringent conditions for 3P absorption, the absorption coefficient is relatively small. In particular, the measured 3P absorption cross-section for the $CsPbBr_3$ QDs is about three orders of magnitude higher than that of conventional metal-sulfide based QDs,[4,13,14] indicating the possibility of achieving ultralow-threshold 3PP lasing.

To gain a deeper understanding of the selection rules that govern the 2P and 3P absorption processes in the cubic-phase $CsPbBr_3$ PQD, we calculated its quasi-particle band structure using a cubic box model with an infinite potential barrier,[30,31] where the band gap of bulk $CsPbBr_3$ is assumed to be 2.25 eV.[32] The effective masses of electron and hole are $0.15m_0$ and $0.14m_0$, respectively, where m_0 is the electron mass in vacuum.[33] In our model, we consider the first four levels with finite degeneracy, i.e., one (111) *S* state and three *P* states: (211), (121), and (112), where the three numbers in each parenthesis represent the nodal planes associated with the spatial confinement along *x*, *y*, and *z* axes (the growth directions of the PQDs), respectively. The orbital quantum numbers of each exciton state are identified by the character of its real-space wavefunction shown in Figure 1f (calculation details in Supporting Information). The calculated energies for the excitonic transitions $S_h \rightarrow S_e$ and $S_h \rightarrow P_e$ in a 9.2 nm $CsPbBr_3$ QD are 2.434 and 2.523 eV, agreeing well with the values extracted from the experimental spectra in Figure 1c,d. The calculated intra-band *S*-*P* energy spacing is 89 meV for the electron and 95 meV for the hole (see Figure S4, Supporting Information), both close to the experimental results. Note that the *S*–*P* energy differences for the electron and hole are nearly identical. Thus, the transitions $S_h \rightarrow P_e$ and $P_h \rightarrow S_e$ cannot be resolved in 1P absorption. Based on the linear and nonlinear absorption results in Figure 1c–e, we illustrate the full scenario of 2P- and 3P-pumped excitonic transitions in the $CsPbBr_3$ PQDs in Figure 1g: upon exciting an electron to the P_e state through either a 2P (from S_h) or 3P (from P_h) process, it relaxes toward the lowest-energy excited state S_e through vibration damping, and then decays to the ground state S_h through excitonic recombination, giving rise to either 2P or 3P PL. It is important to point out that the resonant 3P excitation from S_h to S_e is the most

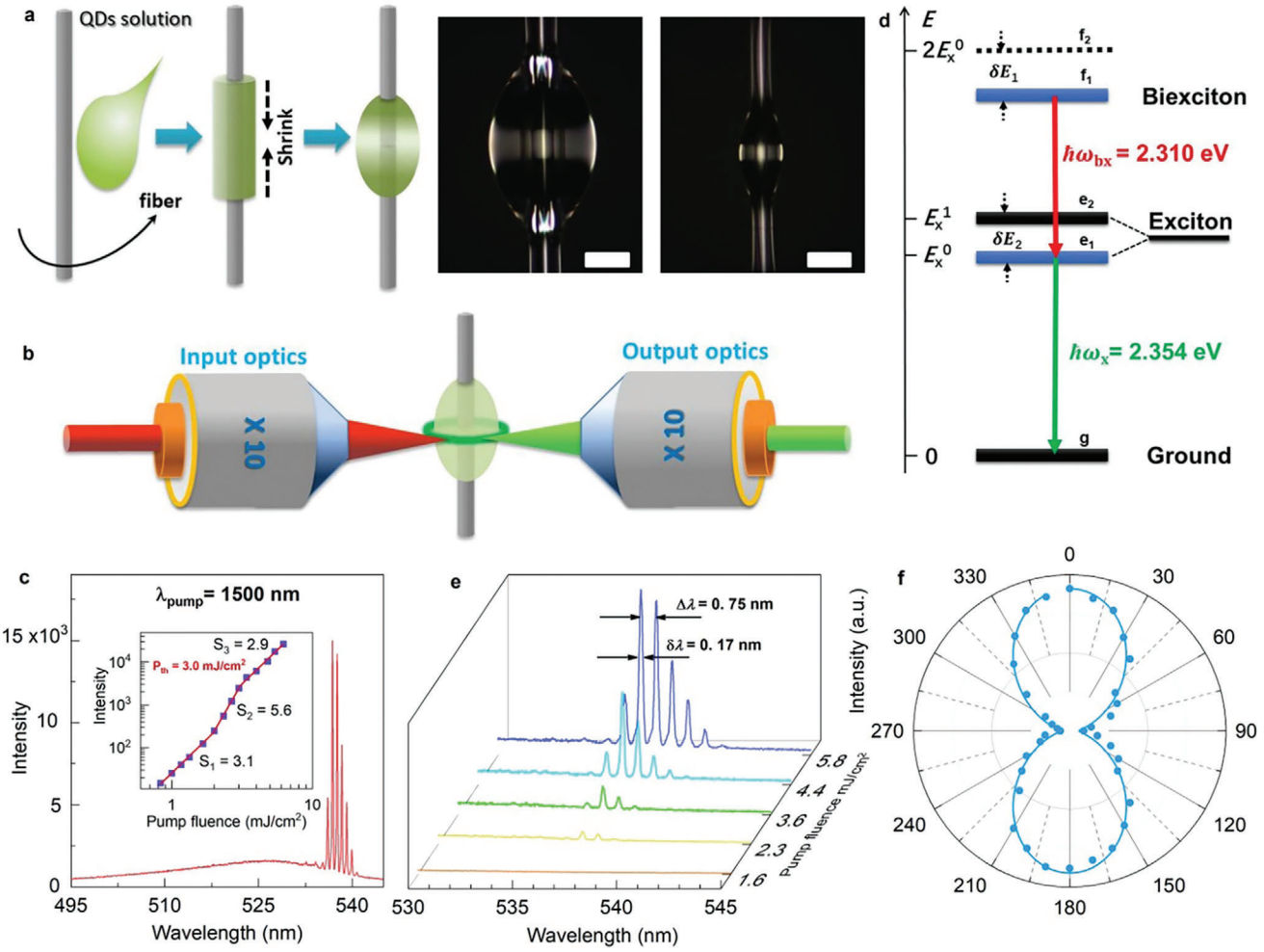

Figure 2. a) Schematic procedure of fabricating bottle-like microcavities as well as two typical microscopic images of the fabricated microcavities (scale bar is 50 μm). b) Schematic diagram of the lasing measurements setup. c) A typical 3PP lasing spectrum from an 88 μm diameter microcavity. The inset shows the log-log plots of integrated emission intensities versus pump fluence. d) Level diagram for the lasing produced from the Biexciton → Exciton transition (red arrow). Green arrow denotes the transition responsible for PL. δE_1 and δE_2 give the biexciton binding energy and single-exciton Stokes shift, respectively. e) 3PP lasing spectra versus pump fluence. f) Integrated lasing intensity as a function of the angle (θ) between the fibre length direction and the transmission axis of a polarizer in front of the detector. The solid line represents a $\cos^2\theta$ fit to the experimental data (solid dots).

efficient multi-photon pumping process among all the possibilities depicted in Figure 1g due to two key advantages: (i) The minimized quantum defect between resonant 3P pumping and emission involves lowest phonon emission and is the most efficient optical pumping process; (ii) the involvement of only the ground state of conduction band with the longest lifetime is the easiest to achieve population inversion.

2.2. Fabrication of the Microcavities and the Lasing Measurement

We fabricated "bottle-like" polymeric microcavities by dispensing a droplet of a PMMA and epoxy resin containing solution of the PQDs onto a commercial optical fiber, as we show in the left panel of **Figure** 2a (see details in Materials and methods). As seen from the right panel of Figure 2a, the optical images indicate a circular symmetry along the equator of the microcavities, which are equatorial whispering-gallery modes as discussed later on. We validated the lasing action of the fabricated microcavities using a fluorescence microscope system (see Figure 2b). The input beam was focused onto the equator of the bottle-like microcavity and the lasing emissions were collected by an objective coupled to a fiber spectrometer. In order to better showcase the WGM microcavities as prepared, we measured micrographs of the WGM microcavities under two-photon excitation. From the image in Figure S5 (Supporting Information), it can be observed that the QDs are uniformly distributed inside the microcavity.

As shown in Figure 2c, the 3PP lasing emission was measured on an 88 μm-diameter microcavity. The profile of the lasing peaks show a red-shift with respect to the spontaneous emission, suggesting that the lasing emission originates from the biexcitonic recombination.[11] According to the energy difference between spontaneous emission maximum and lasing peak, the

biexciton binding energy is derived as 44 meV, which is close to the value reported previously in $CsPbBr_3$ PQDs.[15] Such large binding energy in $CsPbBr_3$ PQDs allows the biexciton states to survive at room temperature (thermal energy ≈ 26 meV at 300 K). Moreover, the large redshift can reduce the detrimental reabsorption loss in $CsPbBr_3$ PQDs. The light input–output curve versus pump fluence is shown in log–log plot in the inset of Figure 2c, where the well-defined nonlinear power-dependent behavior within three distinct regimes can be recognized from ASE threshold (P_a = 2.1 mJ cm^{-2}) and lasing threshold (P_{th} = 3.0 mJ cm^{-2}). The cubic power dependence (with slope of 3.1) obtained below ASE threshold is attributed to spontaneous emission following 3P absorption, as illustrated in Figure 1g. The onset of lasing at higher 3PP fluence was accompanied by a sixth power dependence (with slope of 5.6), and the fitted exponents to the output intensities under 3PP confirm the biexciton gain model.[5] At higher pump intensities, the input–output curve is again approximately cubic (with slope of 2.9), signifying the gain saturation of the $CsPbBr_3$ PQDs due to the twofold-degenerate S exciton state. For comparison, the log–log plot of lasing emission under 2PP is provided in Figure S7 (Supporting Information), where the observed lasing threshold (P_{th} = 0.6 mJ cm^{-2}) is five times smaller than that of the 3PP lasing.

Figure 2d illustrates the level diagram indicating the channels for lasing and PL emissions in the PQDs. The single-exciton Stokes shift δE_2 from the phonons interacting with the electrons in the conduction band and the exciton-exciton binding δE_1 leading to the biexciton state, e.g., $\delta E_1 \simeq 44$ meV and $\delta E_2 \simeq 126$ meV in the $CsPbBr_3$ PQDs, causes the quantum defect. The lasing efficiency within conventional paradigms is mostly bottlenecked from the phonon-induced exciton relaxation as a result of the quantum defect. Since the 3PP pumping has the energy triplicated exactly the same as the $E_x{}^1$, the energy dissipation through phonons can be minimized. In this sense, the quantum defect of our laser is minimized to its lowest value composing only the biexciton binding energy δE_1 and the inherent Stokes shift energy δE_2. We will elaborate this later on.

Figure 2e shows the evolution of 3PP lasing emissions against the pump fluence. As the pump fluence is over ASE threshold (P_a = 2.1 mJ cm^{-2}), sharp peaks with a linewidth of 0.17 nm emerges and grows rapidly in further when exceeding the lasing threshold (P_{th} = 3.0 mJ cm^{-2}). The lasing peaks are slightly blue-shifted as the pump fluence increases, probably due to the state-filling effect.[34] The bottle-like microcavity with cylindrical symmetry could support two types of high-Q factor lasing modes: one is the traditional equatorial whispering-gallery mode where light propagates in closed loop around the equator; the other is called "bottle mode" where light spirals back and forth along the resonator axis between two turning points.[35] Our microcavity is a fiber-stand polymer resonator, where bottle mode is not allowed. A periodic pattern of rare-earth upconversion nanoparticles-based lasing has been observed in similar microcavities,[36,37] which demonstrated the support of whispering-gallery-mode lasing at a thin equatorial ring near the surface of the microcavity. For a whispering-gallery mode, the mode spacing ($\Delta\lambda$) of the two adjacent maxima is determined by the following equation

$$\Delta\lambda = \frac{{\lambda_0}^2}{\pi D_m n_{eff}} \quad (1)$$

where λ_0 is the peak wavelength of the lasing spectrum, D_m is the external diameter of microcavity and n_{eff} (= 1.46) is the effective refractive index of the PMMA polymer.[38,39] The $\Delta\lambda$ of the 88 μm microcavity was calculated to be 0.72 nm from Equation (1), in good agreement with the measured value of 0.75 nm that corroborates the fact that our bottle-like microcavity supports whispering-gallery mode lasing.

The polarization of lasing emission was analyzed by putting a polarizer in front of the detector and setting the polarizer's transmission axis parallel to the optical fiber (corresponding to rotation angle of zero). The integrated intensities of lasing peaks as a function of rotation angle are shown in Figure 2f. The data fits well with Malus' law,[39] and the lasing polarization is consequently identified to be transverse magnetic (TM) modes. The polarization is quantified with a large polarization extinction ratio of 93%, defined as the ratio of lasing intensities in the two polarization directions. Moreover, numerical calculation of the electromagnetic field distribution of the TM modes inside the microcavity was carried out using the finite element method (supported from COMSOL Multiphysics). As seen in Figure S8a (Supporting Information), cross-sectional view of simulated electric field profiles for the first and second order whispering-gallery modes of the microcavity were calculated according to the circular symmetry of the equator on the microcavity. In order to understand the field distribution better, intensity profiles of the first and the second orders in radial direction are plotted in Figure S8b (Supporting Information). Notably, integration of the mode distribution curve shows that up to 99% of optical energy is confined inside the microcavities for both cases, which account for the low loss WGM lasing.

2.3. Exciton Resonance Effect and Optical Net Gain Evolution

The wavelength-dispersive pump thresholds of the 2PP and 3PP lasing is shown in **Figure 3**a,b. Clearly, the pump thresholds reach minima when the 2PP and 3PP energies approach the S and P exciton states at which the nonlinear absorption cross-sections exhibit maximum. The 2P and 3P absorptions of $CsPbBr_3$ PQDs are significantly leveraged through matching the input excitation energy with an exciton resonance, thus leading to low-threshold excitonic lasing. To our knowledge, the observed threshold of ≈3.0 mJ/cm^2 here may be the lowest value reported for 3PP lasers with inorganic semiconductor QDs, five times lower than that with CdSe/CdS/ZnS QDs (see Table S1, Supporting Information). Additionally, Figure 3a,b illustrate the wavelength-dispersive intensities of 2PP and 3PP lasing emissions, where the lasing intensities could retain near-to-90% and 80% of their initial values over 10^7 laser pulses (corresponding to 2 h of excitation), respectively (see Figure S9, Supporting Information). As the infrared pumping energy approaches the PQD exciton radiation energy under the quantum-defect-minimized pumping, heat generation can be greatly reduced because the waste heat per photon is reduced (to 12.4% for 2PP lasing and 6.8% for 3PP lasing, see Table S1, Supporting Information). This can significantly inhibit the lattice temperature rising of the PQDs and thus prevent potential photothermal damage, thereby improving the stability of laser devices.

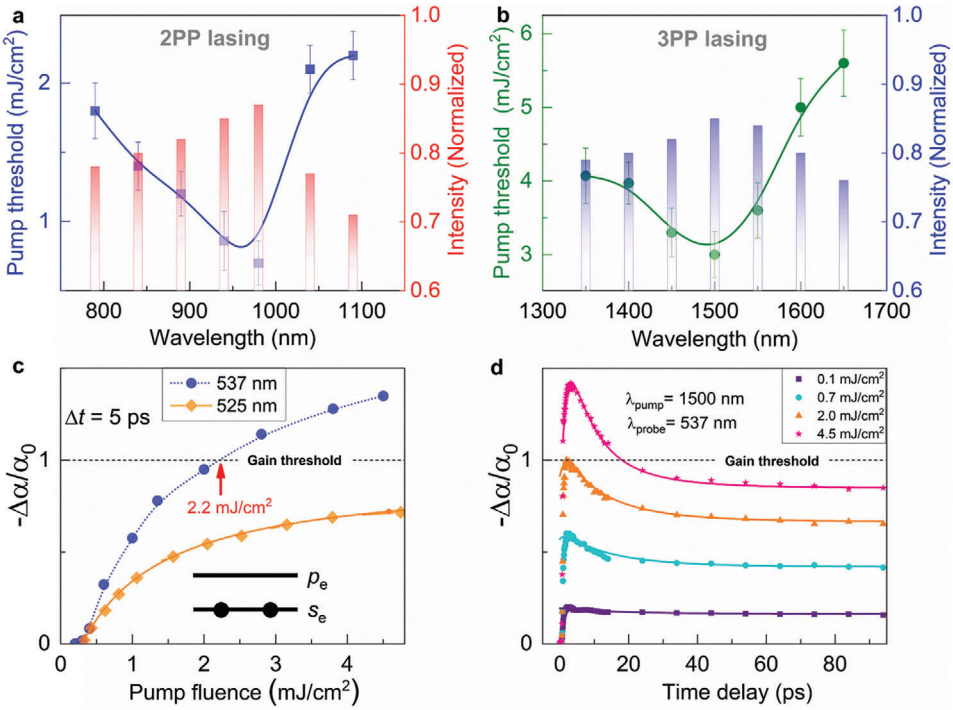

Figure 3. a,b) Wavelength-dispersive pump thresholds and the stability tests by 2P (a) and 3P (b) absorption. c) Bleaching amplitude of the $CsPbBr_3$ PQDs at wavelengths 525 nm (orange squares) and 537 nm (purple dots) as a function of pump fluence (pump-probe delay is 5 ps). The solid lines are fitted with the two-fold state-filling model.[40] d) Transient absorption kinetics of the PQDs for various 1500 nm pump fluence. The solid lines are fitting by Equation (2). The dashed black lines in (c) and (d) denote the optical gain threshold.

To track the evolution of 3PP optical net gain in $CsPbBr_3$ PQDs, we employed ultrafast transient absorption spectroscopy. Optical net gain (i.e., negative absorption) corresponds to pump-induced absorption bleaching with a magnitude that is greater than absorption in the ground state which can be manifested as $-\Delta\alpha/\alpha_0 > 1$, where α_0 is the linear absorbance at probe wavelength.[41] As seen in Figure 3c, the value of $-\Delta\alpha/\alpha_0$ measured at a delay of 5 ps at wavelengths of 537 nm (in coincide with the lasing peaks) shows the emergence of an optical net gain when pump fluence exceeds 2.2 mJ cm^{-2}, yielding an average exciton population of 1.5, close to the ASE threshold (2.1 mJ cm^{-2}) observed in Figure 2c. Besides, the value of $-\Delta\alpha/\alpha_0$ probed at 525 nm (coinciding with the maximum of spontaneous emission) is below the gain threshold and got saturated. This is attributed to the finite degeneracy in the S exciton state.[41] Figure 3d shows the ultrafast kinetics of $-\Delta\alpha/\alpha_0$ of $CsPbBr_3$ QDs at the probe wavelengths of 537 nm, revealing that the excitonic radiation reaches an optical net gain above the ASE threshold, with the population inversion lasting for 18 ps for lasing emissions.

To gain a deeper understanding of the present time-resolved measurement results, a microscopic model for the pump-probe signal incorporating the density matrix dynamics is developed.[42] The quantum master equation for the density matrix of a four-level model describes the fast-evolving dynamics of population and quantum coherence, responsible for the time-resolved pump-probe measurements and the lasing dynamics. From the experimental schemes, the transmission of the probe pulse was measured, giving the signal $S_{pp}(\omega, t) = \mathrm{Im}[E^*_{pr}(\omega)P(\omega)]$ where $E_{pr}(\omega)$ is the Fourier component of the probe with positive frequency and $P(\omega)$ is the polarization of the PQDs. Some algebra leads to the signal measured at $\lambda_{probe} = 537$ nm corresponding to the $f_1 \rightarrow e_1$ transition in Figure 2d:

$$S_{pp}(\lambda_{probe}, t) = \frac{2|\varepsilon(\omega_{f_1e_1} - \upsilon)|^2}{\gamma_{f_1e_1}} \left[\frac{\rho^{(0)}_{f_2f_2}}{1-x} \left(e^{-\gamma_E t} - e^{-\frac{\gamma_E t}{x}} \right) + \rho^{(0)}_{e_2e_2} e^{-\gamma_{nr} t} - 1 \right] \quad (2)$$

where $\varepsilon(\omega - \upsilon)$ gives the Fourier component of the probe pulse envelop and $\gamma_{f_1e_1}$ yields the line-broadening of the signal, $x = \gamma_E/\Gamma$. γ_{nr}, γ_E and Γ represent the rates of phonon-induced non-radiative decay of single exciton, biexciton damping and two-exciton decay, respectively. $\rho^{(0)}_{e_2e_2}$ and $\rho^{(0)}_{f_2f_2}$ are the initial populations of single and two-exciton states created by the femtosecond pump pulse, as illustrated in Figure 2d. All the theoretical details are given in SI.

The solid lines in Figure 3d illustrate the time dependence of the signal produced from Equation (2) in comparison with the experimental measurements. Notably, the transmission of the probe field exhibits a sharp rising edge during the first few hundred femtoseconds, before the decay. This is prominent when lasing emerges under an intense pumping, and can be attributed to the fast population relaxation from the two-exciton metastable state to the biexciton state. Basically, there are two channels for populating the biexciton state f_2 which trade off with each other: one is the pumping from the metastable state f_1 while the other is the exciton-exciton annihilation (EEA).[43] As revealed in Figure 3d, the microscopic model produces the results in perfect

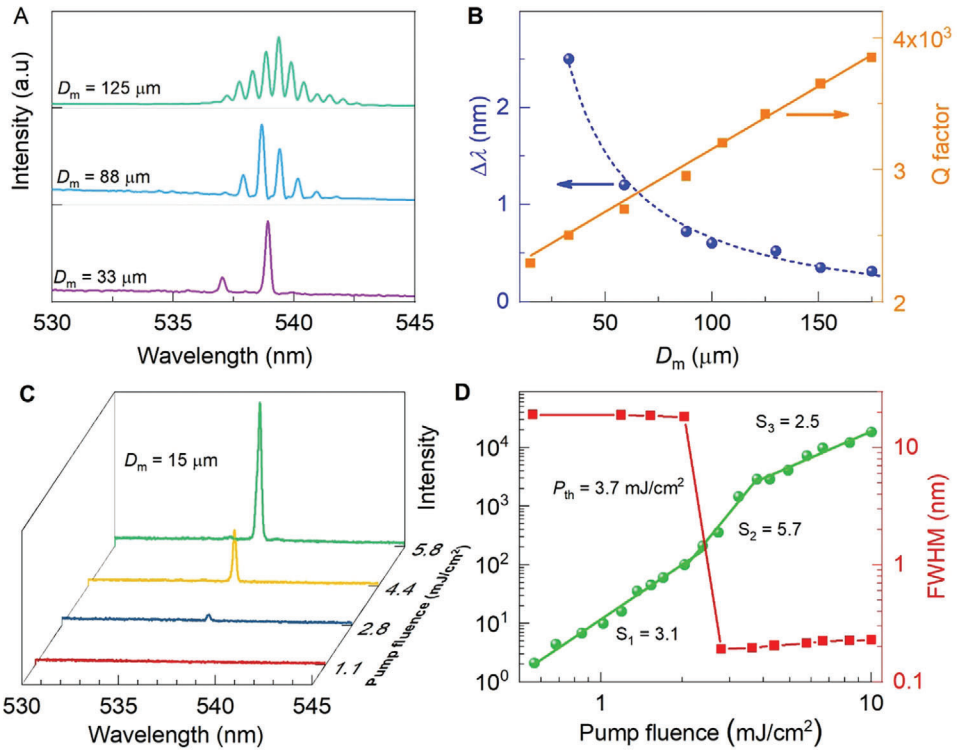

Figure 4. a) Three-photon-pumped lasing spectra collected for microcavities with 125, 88 and 33 μm in diameter. b) The measured $\Delta\lambda$ and Q-factor as a function of D_m. The Q factor is defined as the ratio of the resonant frequency (λ_0) to its FWHM ($\delta\lambda$). The data can be well fitted to a single-exponential function (dashed line) and a linear function (solid line), respectively. c) Single-mode lasing spectra collected from a 15 μm diameter microcavity under varied pump fluence. d) The log-log plots of integrated lasing emission intensities and linewidths versus pump fluence of the single-mode lasing.

agreement with the experimental measurements, provided that a typical set of relaxation parameters $\gamma_E^{-1} = 7$ ps, $\Gamma^{-1} = 0.2\gamma_E^{-1}$, $\gamma_{nr}^{-1} = 2.5\gamma_E^{-1}$ applicable for all the pumping intensities. This indicates two fitting parameters only: $\rho_{e_2e_2}^{(0)}$ and $\rho_{f_2f_2}^{(0)}$ subject to the pumping intensities. The fitting results are summarized in Table S1 (Supporting Information). From the microscopic model, the lifetime of the optical net gain is manifested to be ≈18 ps. It is worth noting that the population of biexciton state is upper bounded by the fast relaxation of metastable state. This is proved in a math rigor and is thus the bottleneck for optimizing the optical gain efficiency in the present experiment.

2.4. Tuning the Microcavities for Single-Mode Lasing

Finally, we demonstrated that the 3PP exciton laser could be switched between multi- and single mode by simply adjusting the cavity diameter with an easy-to-implement all-solution-processed method. **Figure** 4a presents the reduced mode number with reducing the microcavity diameter. The mode spacing as a function of D_m are presented in Figure 4b, where the measured values of $\Delta\lambda$ versus D_m can be well fitted from Equation (1). The fitting yields a value of $n_{eff} = 1.47$, which is close to the estimated value of 1.46, confirming the WGM lasing mechanism. In addition, the Q-factors increase linearly with the D_m as shown in Figure 4b, because the scatter loss is linearly scaled with the D_m,[39] suggesting that larger microcavities perform better in light confinement than that of smaller ones. The maximum Q-factors (> 3000) of our microlaser are higher than the reported ones using perovskite nanoplatelets and nanowires,[44–46] manifesting that the low scattering loss is well achieved with our all-solution-processed method.

The single-mode lasing was demonstrated in a small microcavity with $D_m = 15$ μm (see Figure 4c). The single-mode emission is a result of a relatively large mode spacing (4.2 nm) with respect to the global width of lasing spectrum in $CsPbBr_3$ QDs. This S-like log–log plot in Figure 4d clearly shows a transition from a spontaneous emission to an ASE, and finally to a single-mode lasing emission. As shown in Figure 4d, the full width at half maximum at 537.6 nm narrows rapidly from 19 to 0.19 nm as increasing the 3PP fluence around the onset power. The pump threshold for single-mode lasing was found to be 3.7 mJ cm^{-2}. The slightly increased pump threshold with respect to that of the multimode lasing is attributed to the large curvature loss in small diameter microcavities.

3. Conclusion

We realize 3PP lasing of all-inorganic $CsPbBr_3$ PQDs in a WGM microcavity and achieve a record low threshold of 3 mJ cm^{-2} by quantum-defect-minimized resonant pumping. Based on the wavelength-dispersive open-aperture *Z*-scan nonlinear spectroscopy, the parity-allowed excitonic transitions were precisely measured, which are consistent with the quantum mechanical

calculation using a cubic box model. Moreover, the optical net gain in $CsPbBr_3$ PQDs was observed by ultrafast transient absorption spectroscopy when pump fluence is above 2.2 mJ cm^{-2}, and it could survive as long as 18 ps for the lasing emission. A four-level model incorporating quantum master equation produces the signal in perfect agreement with the ultrafast transient absorption measurement results, where the intrinsic parameters of excitons in the $CsPbBr_3$ PQDs were found to be applicable for all the pump fluences used in experiments. An all-solution-processed method was used to fabricate the microcavities to confine the $CsPbBr_3$ PQDs for lasing emissions. Such methodology has enabled us to readily incorporate the PQDs into the polymeric microcavities, which allows flexible modulation of the lasing characters. Finally, we demonstrated the switch of 3PP exciton laser between multi- and single mode by simply adjusting the cavity diameter with the easy-to-implement all-solution-processed method. The demonstration of 3PP microlaser with a record threshold marks a major step towards inorganic semiconductor PQDs on-chip optoelectronics for high-performance near-infrared biophotonics and optical communication.

Supporting Information

Supporting Information is available from the Wiley Online Library or from the author.

Acknowledgements

The authors acknowledge the financial support from the Research Grants Council of Hong Kong through an NSFC/RGC CRS grant (CRS_CityU104/23) and an Early Career Scheme grant (21302721), the Outstanding Youth Science Fund of Heilongjiang University (JCL202303), the Outstanding Youth Fund of Heilongjiang Province (YQ2020A006, YQJH2023142), the City University of Hong Kong through a Central Research Facility grant (9360165), the Centre for Functional Photonics of City University of Hong Kong, the Hong Kong Institute for Advanced Study of City University of Hong Kong, and the Hong Kong Branch of National Precious Metals Material Engineering Research Center (ITC Fund). Jianhui Sun also thanks Dr. Xin Gai for the useful discussions.

Conflict of Interest

The authors declare no conflict of interest.

Author Contributions

J.S. and D.Y.L. conceived the idea of this work. J.S. performed materials synthesis, device fabrication, and lasing measurement, and prepared the manuscript. Z.Z. performed the microscopic model calculation. Y.C. simulated the electromagnetic field distribution of the WGM cavity. M.Q. performed the quantum mechanical calculations of excitonic states. D.Y.L. guided the overall project and revised the manuscript. W.J., C.Z.N., H.J.S., and A.K.-Y.J. involved in the discussion and polished the manuscript. All authors reviewed the manuscript.

Data Availability Statement

The data that support the findings of this study are available from the corresponding author upon reasonable request.

Keywords

perovskite quantum dots, quantum defect, quantum master equation, three-photon-pumped excitonic lasing, transient absorption spectroscopy

Received: March 7, 2024
Published online: March 18, 2024

[1] G. S. He, P. P. Markowicz, T.-C. Lin, P. N. Prasad, *Nature* **2002**, *415*, 767.
[2] U. Resch-Genger, M. Grabolle, S. Cavaliere-Jaricot, R. Nitschke, T. Nann, *Nat. Methods* **2008**, *5*, 763.
[3] D. Pan, J. Zhang, Z. Li, M. Wu, *Adv. Mater.* **2010**, *22*, 734.
[4] J. H. Yu, S.-H. Kwon, Z. Petrášek, O. K. Park, S. W. Jun, K. Shin, M. Choi, Y. Il Park, K. Park, H. Bin Na, N. Lee, D. W. Lee, J. H. Kim, P. Schwille, T. Hyeon, *Nat. Mater.* **2013**, *12*, 359.
[5] M. Li, M. Zhi, H. Zhu, W.-Y. Wu, Q.-H. Xu, M. H. Jhon, Y. Chan, *Nat. Commun.* **2015**, *6*, 8513.
[6] H. He, E. Ma, Y. Cui, J. Yu, Y. Yang, T. Song, C. De Wu, X. Chen, B. Chen, G. Qian, *Nat. Commun.* **2016**, *7*, 11087.
[7] E. P. Perillo, J. W. Jarrett, Y.-L. Liu, A. Hassan, D. C. Fernée, J. R. Goldak, A. Bonteanu, D. J. Spence, H.-C. Yeh, A. K. Dunn, *Light Sci. Appl.* **2017**, *6*, e17095.
[8] K. C. Kao, G. A. Hockham, *Elektron* **1997**, *14*, 1151.
[9] C. DeCusatis, *Fiber Optic Data Communication: Technological Trends and Advances*, ACADEMIC PRESS, New York, **2002**.
[10] Y. Wang, X. Li, X. Zhao, L. Xiao, H. Zeng, H. Sun, *Nano Lett.* **2016**, *16*, 448.
[11] Y. Xu, Q. Chen, C. Zhang, R. Wang, H. Wu, X. Zhang, G. Xing, W. W. Yu, X. Wang, Y. Zhang, M. Xiao, *J. Am. Chem. Soc.* **2016**, *138*, 3761.
[12] J. Pan, S. P. Sarmah, B. Murali, I. Dursun, W. Peng, M. R. Parida, J. Liu, L. Sinatra, N. Alyami, C. Zhao, E. Alarousu, T. K. Ng, B. S. Ooi, O. M. Bakr, O. F. Mohammed, *J. Phys. Chem. Lett.* **2015**, *6*, 5027.
[13] Y. Wang, V. D. Ta, Y. Gao, T. C. He, R. Chen, E. Mutlugun, H. V. Demir, H. D. Sun, *Adv. Mater.* **2014**, *26*, 2954.
[14] B. Guzelturk, Y. Kelestemur, K. Gungor, A. Yeltik, M. Z. Akgul, Y. Wang, R. Chen, C. Dang, H. Sun, H. V. Demir, *Adv. Mater.* **2015**, *27*, 2741.
[15] Y. Wang, X. Li, J. Song, L. Xiao, H. Zeng, H. Sun, *Adv. Mater.* **2015**, *27*, 7101.
[16] S. Yakunin, L. Protesescu, F. Krieg, M. I. Bodnarchuk, G. Nedelcu, M. Humer, G. De Luca, M. Fiebig, W. Heiss, M. V. Kovalenko, *Nat. Commun.* **2015**, *6*, 8056.
[17] S. Li, D. Lei, W. Ren, X. Guo, S. Wu, Y. Zhu, A. L. Rogach, M. Chhowalla, A. K. Y. Jen, *Nat. Commun.* **2020**, *11*, 1192.
[18] J. Chen, W. Du, J. Shi, M. Li, Y. Wang, Q. Zhang, X. Liu, *InfoMat* **2020**, *2*, 170.
[19] D. Englund, A. Majumdar, A. Faraon, M. Toishi, N. Stoltz, P. Petroff, J. Vučković, *Phys. Rev. Lett.* **2010**, *104*, 073904.
[20] J. Petit, P. Goldner, B. Viana, *Opt. Lett.* **2005**, *30*, 1345.
[21] N. Ter-Gabrielyan, V. Fromzel, T. Lukasiewicz, W. Ryba-Romanowski, M. Dubinskii, *Opt. Lett.* **2011**, *36*, 1218.
[22] M. Kahle, J. Körner, J. Hein, M. C. Kaluza, *Opt. Laser Technol.* **2017**, *92*, 19.
[23] Q. A. Akkerman, V. D'Innocenzo, S. Accornero, A. Scarpellini, A. Petrozza, M. Prato, L. Manna, *J. Am. Chem. Soc.* **2015**, *137*, 10276.
[24] L. Protesescu, S. Yakunin, M. I. Bodnarchuk, F. Krieg, R. Caputo, C. H. Hendon, R. X. Yang, A. Walsh, M. V. Kovalenko, *Nano Lett.* **2015**, *15*, 3692.
[25] D. Rossi, H. Wang, Y. Dong, T. Qiao, X. Qian, D. H. Son, *ACS Nano* **2018**, *12*, 12436.

[26] G. Nootz, L. A. Padilha, P. D. Olszak, S. Webster, D. J. Hagan, E. W. Van Stryland, L. Levina, V. Sukhovatkin, L. Brzozowski, E. H. Sargent, *Nano Lett.* **2010**, *10*, 3577.
[27] Z. Ye, T. Cao, K. O'Brien, H. Zhu, X. Yin, Y. Wang, S. G. Louie, X. Zhang, *Nature* **2014**, *513*, 214.
[28] M. Allione, A. Ballester, H. Li, A. Comin, J. L. Movilla, J. I. Climente, L. Manna, I. Moreels, *ACS Nano* **2013**, *7*, 2443.
[29] J. J. Peterson, L. Huang, C. Delerue, G. Allan, T. D. Krauss, *Nano Lett.* **2007**, *7*, 3827.
[30] E. Dekel, D. Gershoni, E. Ehrenfreund, D. Spektor, J. M. Garcia, P. M. Petroff, *Phys. Rev. Lett.* **1998**, *80*, 4991.
[31] H. Tong, M. W. Wu, *Phys. Rev. B – Condens. Matter Mater. Phys.* **2011**, *83*, 61.
[32] C. C. Stoumpos, C. D. Malliakas, J. A. Peters, Z. Liu, M. Sebastian, J. Im, T. C. Chasapis, A. C. Wibowo, D. Y. Chung, A. J. Freeman, B. W. Wessels, M. G. Kanatzidis, *Cryst. Growth Des.* **2013**, *13*, 2722.
[33] A. Swarnkar, R. Chulliyil, V. K. Ravi, M. Irfanullah, A. Chowdhury, A. Nag, *Angew. Chemie – Int. Ed.* **2015**, *54*, 15424.
[34] Q. Zhang, S. T. Ha, X. Liu, T. C. Sum, Q. Xiong, *Nano Lett.* **2014**, *14*, 5995.
[35] M. Sumetsky, *Opt. Lett.* **2004**, *29*, 8.
[36] H. Zhu, X. Chen, L. M. Jin, Q. J. Wang, F. Wang, S. F. Yu, *ACS Nano* **2013**, *7*, 11420.
[37] X. Chen, L. Jin, W. Kong, T. Sun, W. Zhang, X. Liu, J. Fan, S. F. Yu, F. Wang, *Nat. Commun.* **2016**, *7*, 10304.
[38] F. Gu, F. Xie, X. Lin, S. Linghu, W. Fang, H. Zeng, L. Tong, S. Zhuang, *Light Sci. Appl.* **2017**, *6*, e17061.
[39] V. Duong Ta, R. Chen, L. Ma, Y. Jun Ying, H. Dong Sun, *Laser Photon. Rev.* **2013**, *7*, 133.
[40] J. Sun, D. Zhu, J. Zhao, M. Ikezawa, X. Wang, Y. Masumoto, *Appl. Phys. Lett.* **2014**, *104*, 2012.
[41] V. I. Klimov, A. A. Mikhailovsky, S. Xu, A. Malko, J. A. Hollingsworth, C. A. Leatherdale, H. J. Eisler, M. G. Bawendi, *Science* **2000**, *290*, 314.
[42] Z. Zhang, K. Wang, Z. Yi, M. S. Zubairy, M. O. Scully, S. Mukamel, *J. Phys. Chem. Lett.* **2019**, *10*, 4448.
[43] Z. Zhang, P. Saurabh, K. E. Dorfman, A. Debnath, S. Mukamel, *J. Chem. Phys.* **2018**, *148*, 74302.
[44] W. Zhang, L. Peng, J. Liu, A. Tang, J. S. Hu, J. Yao, Y. S. Zhao, *Adv. Mater.* **2016**, *28*, 4040.
[45] Q. Zhang, S. T. Ha, X. Liu, T. C. Sum, Q. Xiong, *Nano Lett.* **2014**, *14*, 5995.
[46] S. W. Eaton, M. Lai, N. A. Gibson, A. B. Wong, L. Dou, J. Ma, L.-W. Wang, S. R. Leone, P. Yang, *Proc. Natl. Acad. Sci* **2016**, *113*, 1993.